IEEE Robotics and Automation Letters (RA-L) paper, presented at ICRA 2024, Yokohama, Japan. Cite as RA-L paper.

Integrated Magnetic Location Sensing and Actuation of Steerable Robotic Catheters for Peripheral Arterial Disease Treatment

Jingjie Wu[1], *Student Member, IEEE*, Kevin Yu[2], Ithza Lopez[2], Alexa Aguilar Izquierdo[2], Hamidreza Saber[3], Farshid Alambeigi[2,†], *Member, IEEE*, and Lei Zhou[1,†], *Member, IEEE*

***Abstract*—Magnetically steerable robotic catheters (MSRC) are a promising technology for percutaneous endovascular intervention (PEI) procedures to treat peripheral arterial diseases (PAD), where magnetic actuation is used to steer the catheter tip during navigation. However, today's MSRC systems require fluoroscopic imaging for catheter location sensing during the procedure, which risks creating radiation-induced injuries to both the patient and the radiologist. Aiming to reduce the duration of x-ray radiation in interventions using MSRCs, this letter introduces a new type of steerable robotic catheter system that integrates magnetic location sensing and magnetic actuation. The proposed catheter uses a magnetic tip to enable steering by external electromagnetic actuators. In addition, a cylindrical array of magnetic sensors is used to measure the field from the catheter tip to enable real-time catheter location estimation. To enable improved localization accuracy, a novel nested calibration algorithm for sensor positions and magnet dipole strength is introduced. This letter further proposes a novel integration method for magnetic actuation and magnetic location sensing in MSRC systems, where fluoroscopic imaging is only required during catheter steering at bifurcations in the vasculatures, which effectively reduces x-ray radiation in the navigation process of catheters. The proposed methodology is tested with an MSRC prototype, where a ring-shaped magnet (3 mm OD, 1.6 mm ID, 6 mm length) is arranged at the catheter tip for actuation and location sensing. The magnet location estimation algorithm is implemented for real-time visual feedback to the operator with a low latency of 400 ms. Experiments show that an average position estimation error of 0.95 mm can be achieved after calibrating the system using the proposed algorithm. The prototype catheter can successfully navigate through phantoms of vasculatures under a combination of magnetic steering and magnetic location sensing, which shows the excellent potential of the proposed framework for reducing x-ray exposure in PAD interventions.**

***Index Terms*—Medical Robots and Systems, Magnetic Localization, Magnetic Actuation, Continuum Robot.**

I. INTRODUCTION

According to the United States Centers for Disease Control and Prevention, approximately 6.5 million people age 40 and older in the US are suffering from *peripheral arterial disease* (PAD) today [1]. Under this medical condition, the patient's blood vessels in the legs or lower extremities are obstructed or narrowed, which can cause pain, impaired walking, intermittent claudication, and critical limb ischemia in the involved patients [2]. *Percutaneous endovascular intervention (PEI)* is the primary therapy for PAD [3]. In a PEI procedure, the blockage or narrowed part of the blood vessel is first located via fluoroscopic imaging. Then the radiologist inserts a long flexible tube (i.e., a catheter) into the affected blood vessel through a small incision on the femoral artery and carefully steers it to the blocked area under fluoroscopic imaging guidance and using contrast injections. Next, a balloon or a stent is deployed through the catheter to open the occluded vessel and restore normal blood flow.

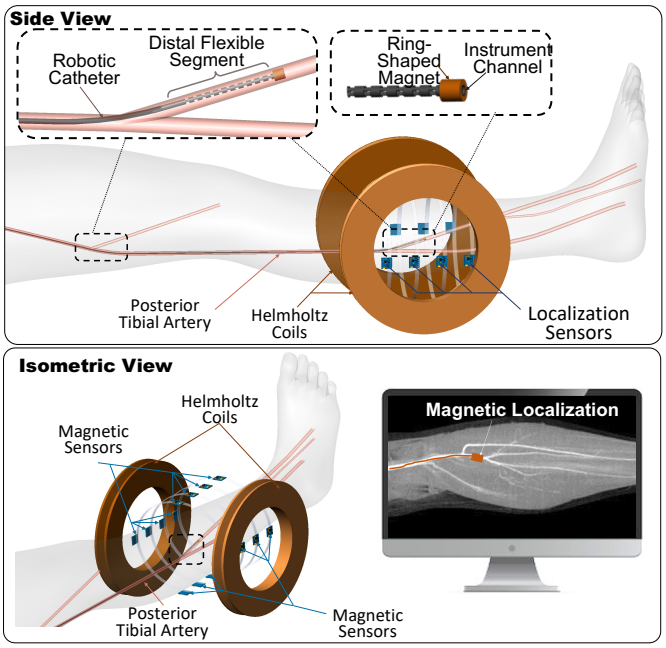

Fig. 1. Conceptual illustration of a magnetically steerable robotic catheter (MSRC) with magnetic localization for peripheral arterial disease (PAD) treatment to reduce x-ray radiation.

Catheters in today's PEI procedures are often passive and cannot be actively steered at their distal ends. Such passive catheters lack the steerability required for quick navigation through complex leg vasculatures with bifurcations and non-uniform branches, making their operation highly demanding and time-consuming [3]. To improve the current workflow, a series of research and development efforts have explored steerable robotic catheters [4], [5]. Among these solutions, magnetically steerable robotic catheters (MSRCs) and guidewires are attracting an increasing interest owing to their advantages

Manuscript received: March 8, 2023; Revised: June 6, 2023; Accepted: June 30, 2023.

This paper was recommended for publication by Editor Pietro Valdastri upon evaluation of the Associate Editor and Reviewers' comments.

† corresponding authors.

[1]J. Wu and L. Zhou are with The University of Wisconsin-Madison, Madison, WI, 53706, USA. Emails: {jingjie.wu, lei.zhou}@wisc.edu.

[2] K. Yu, I. Lopez, A. Aguilar Izquierdo, and F. Alambeigi are with the University of Texas at Austin, Austin, TX, 78712, USA. Emails: {khy, ithza.lopez, alexaizq}@utexas.edu, farshid.alambeigi@austin.utexas.edu.

[3] H. Saber is with the Department of Neurology, Dell Medical School, The University of Texas at Austin, Austin, TX, 78712, USA. Email: hsaber@austin.utexas.edu.

Digital Object Identifier (DOI): see top of this page.

IEEE Robotics and Automation Letters (RA-L) paper, presented at ICRA 2024, Yokohama, Japan. Cite as RA-L paper.

IEEE Robotics and Automation Letters (RA-L) paper, presented at ICRA 2024, Yokohama, Japan. Cite as RA-L paper.

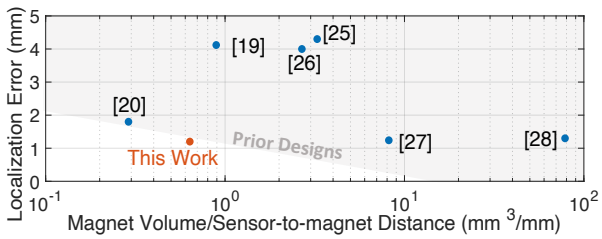

Fig. 2. Comparison in magnet volume/sensor-to-magnet distance $[\mathrm{mm}^3/\mathrm{mm}]$ and tracking accuracy between this work and prior studies.

of allowing robotic-assisted navigation [6], facilitating small form factor and very thin catheters or guidewires [7]–[9], and contactless force and torque transmission without requiring embedded steering mechanisms (e.g., tendons) [10]. Example MSRC systems include the commercial robotic systems *Stereotaxis Niobe* [11] and *CGCI-Maxwell* [12] developed for cardiovascular interventions. More research and development effects for MSRC are summarized in a recent review by Hwang et al [13].

Despite various advantages of today's MSRC systems, the location sensing for the catheter within a vessel still highly depends on fluoroscopic imaging. This imaging modality can put clinicians and patients at risk of increased x-ray radiation exposure, particularly during lengthy procedures, highlighting the need for developing new radiation-free sensing technologies. In MSRCs, a small permanent magnet (PM) is typically arranged at the tip of the catheter to allow for magnetic steering and/or insertion. This design offers the exciting possibility to use the field from the catheter tip for location sensing. Developing an accurate and reliable magnetic localization solution for MSRCs can significantly reduce the fluoroscopic x-ray utilization for catheter navigation, thereby reducing the x-ray exposure and procedural length for these operations.

Magnetic localization, where the magnetic field from a PM or a coil is measured and used to estimate its location and orientation, has demonstrated excellent performance in various applications including industrial robot calibration [14], robotic capsule endoscopes [15], miniature robots [16], [17], and continuum manipulators [18]. Despite these successes, several major technical barriers must be tackled to enable the magnetic localization technology to be successfully used for MSRC systems used in PAD interventions: (i) The catheter must fit within the vessel lumen and thus must have a smaller diameter profile (of 3 mm or smaller), which is significantly smaller than the PM size being used in the prior art. This fact can lead to noises in the sensor signals and thus estimation inaccuracy. Highly sensitive sensors and de-noise algorithms must be used to enable the effective estimation of the catheter location. (ii) The accuracy of the magnet localization directly depends on the accuracy of sensor locations and the model for the PM, which are typically assumed to be known a priori. To address these uncertainties, data-driven calibration algorithms for sensor locations and PM dipole moment have been developed [19]. However, in prior studies, the calibrations of various parametric uncertainties are typically conducted sequentially, which can result in sub-optimal calibration results. New calibration algorithms that address the coupling between the estimation for various uncertainties must be developed to

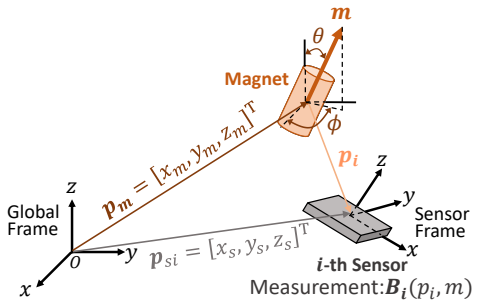

Fig. 3. A schematic diagram showing the variables in magnetic localization.

attain improved magnetic localization accuracy. (iii) In MSRC systems, a strong external magnetic field is needed to actuate the catheter's steering, which is typically from actuation coils [20], [21] or a large piece of PM [6]. Such an actuation field can saturate the magnetic sensors being used for localization. Recent studies have investigated the simultaneous magnetic actuation and localization of continuous robot [22], [23], however, this limitation has not completely been resolved. New algorithms are needed to enable the integration of magnetic actuation and magnetic location sensing to minimize the required duration of fluoroscopic imaging under this limitation. To our knowledge, these three challenges are not addressed in the literature.

The objective of this study is to simultaneously address the above-mentioned limitations and enable the use of magnetic localization for MSRC systems as a means to reduce x-ray radiation in PAD interventions. An MSRC prototype developed by our team [21] is considered in this work, which uses a catheter with a ring-shaped PM (3 mm OD, 1.6 mm ID, 6 mm length) arranged at its tip for magnetic steering. A cylindrical array of highly-sensitive magnetoresistive sensors together with a low-latency magnet location estimator based on the Levenberg-Marquadt (LM) algorithm is proposed to track the location of the catheter tip in real-time. Particularly, to enable improved estimation accuracy while maintaining computational simplicity, a novel nested calibration algorithm for sensor positions and magnetic strength is proposed. This letter further introduces a novel integration method for magnetic actuation and magnetic location sensing in MSRC systems, where fluoroscopic imaging is only required during catheter steering at bifurcations in the vasculatures. Experiments show that an average position estimation error of 1.27 mm can be achieved after calibrating the system using the proposed algorithm. The prototype catheter can successfully navigate into the desired branch of bifurcation with visual feedback using magnetic localization during insertions and a digital microscope during steering, which shows the excellent potential of the proposed framework for reducing x-ray imaging in practical interventions. Compared with recent literature on magnetic localization [18], [19], [24]–[27] (Fig. 2), this work presents an excellent overall performance in terms of magnet volume/sensor-to-magnet distance ratio $[\mathrm{mm}^3/\mathrm{mm}]$ and localization accuracy.

II. Realtime Localization Algorithm

A. Mathematical Model

Figure 3 shows a diagram for the variables used in the magnet localization algorithm. Since PM in an MSRC is small

IEEE Robotics and Automation Letters (RA-L) paper, presented at ICRA 2024, Yokohama, Japan. Cite as RA-L paper.

IEEE Robotics and Automation Letters (RA-L) paper, presented at ICRA 2024, Yokohama, Japan. Cite as RA-L paper.

and magnetic sensors are placed sufficiently far away from the magnet, the PM's flux density at i-th sensor location $\mathbf{B_i} \in \mathbb{R}^3$ can be described by the dipole model [28] as

$$\mathbf{B_i} = \frac{\mu_0}{4\pi}\Big(\frac{3(\mathbf{m}^\top \mathbf{p}_i \cdot \mathbf{p}_i)}{\|\mathbf{p}_i\|^5}\Big) - \frac{\mathbf{m}}{\|\mathbf{p}_i\|^3}\Big) \ , \tag{1}$$

where $\mathbf{m} \in \mathbb{R}^3$ is the magnetic dipole moment vector of the PM, μ_0 is the magnetic permeability of free space, and $\mathbf{p}_i \in \mathbb{R}^3$ is the vector from the center of the magnet to i-th sensor location. The vector $\mathbf{p}_i \in \mathbb{R}^3$ can be calculated via

$$\mathbf{p}_i = \mathbf{p_{s}}_i - \mathbf{p_m}, \tag{2}$$

where $\mathbf{p_{s}}_i = [x_s, y_s, z_s]^\top$ and $\mathbf{p_m} = [x_m, y_m, z_m]^\top$ are the coordinates of i-th sensor and magnet in the global-fixed frame, respectively. The dipole moment vector $\mathbf{m} \in \mathbb{R}^3$ for the PM can be represented as

$$\mathbf{m} = M(\sin\theta\cos\phi\mathbf{i} + \sin\theta\sin\phi\mathbf{j} + \cos\phi\mathbf{k}), \tag{3}$$

where $\mathbf{i}$, $\mathbf{j}$, and $\mathbf{k}$ are the unit vectors in the x, y, and z-axes, respectively; θ and ϕ are the angles of magnet's orientation in a spherical coordinate with its origin at the center of the magnet location, as shown in Fig. 3; M represents the dipole moment strength of the PM, which can be calculated as

$$M = \frac{B_r V_m}{\mu_0}, \tag{4}$$

where B_r is the magnetic remanence of the PM material, and V_m is the volume of the magnet.

Assume the magnetic sensor can measure the magnetic flux density at the sensor location along three perpendicular axes in its sensor-fixed frame. The measured flux density in the sensor frame ${}^{\mathbf{s}}\mathbf{B_i}$ can be calculated as

$${}^{\mathbf{s}}\mathbf{B_i} = \mathbf{T_i}\mathbf{B_i}, \tag{5}$$

where $\mathbf{T_i} \in \mathbb{R}^{3\times3}$ is the rotation matrix between the global coordinate and the i-th sensor-fixed coordinate, Note that all vectors with superscripts "s" represent coordinates in a sensor-fixed frame, while those without a superscript are defined in the global frame.

B. Magnetic Localization Algorithm

This section introduces the magnetic localization algorithm used for the MSRC tip location sensing, which is based on the algorithm introduced in Taylor et al. [25] and is modified to suit the MSRC application.

Based on the dipole model introduced in Section II-A, a nonlinear optimization problem can be formulated and solved to estimate the magnet's position and orientation as

$$\hat{\xi} = \arg\min_{\xi} \sum_{i=1}^{N_s} \|{}^{\mathbf{s}}\mathbf{B_i}(\xi, \mathbf{p_{si}}, M) - {}^{\mathbf{s}}\mathbf{B_i}^{'}\|^2, \tag{6}$$

where $\hat{\xi} = [\hat{\mathbf{p_m}}^\top, \hat{\theta}, \hat{\phi}]^\top \in \mathbb{R}^5$ is a vector of the estimated position and orientation angles for the magnet, N_s is the number of sensor measurements available for the magnetic location estimation, and ${}^{s}B_i^{'}$ is the measurement data from i-th sensor in its individual sensor coordinate frame. In (6), the cost function to be minimized is the sum-of-squared error between the magnetic field prediction from (1) and the measurements.

A number of algorithms have been used to solve this nonlinear optimization problem, such as the steepest gradient descent algorithm and Newton's method. In this work, we selected the Levenberg-Marquardt (L-M) algorithm for solving (6), which is suitable for solving nonlinear least-square problems in real-time [29]. The L-M algorithm utilizes the Jacobian matrix at the current estimation to perform parameter updates in a descent direction iteratively toward a local minimum. A common way to calculate the Jacobian matrix is numerically computing the derivatives by evaluating the prediction error at least once for each parameter, which is computationally expensive and unsuitable for real-time magnetic location estimation. Aiming to achieve minimum latency to allow for real-time localization while attaining acceptable estimation accuracy, an analytical expression of the Jacobian matrix is computed by taking derivatives of the magnetic field prediction in sensor frame (5) with respect to the parameters as

$$\mathbf{J_i} = \mathbf{T}_i \frac{\partial \mathbf{B_i}}{\partial \xi}, \tag{7}$$

where $\mathbf{J_i} \in \mathbb{R}^{3\times5}$ is the Jacobian submatrix corresponding to i-th sensor. The total Jacobian matrix is composed of all Jacobian submatrices $\mathbf{J}_i$ across N_s sensors. The detailed expression of the analytical-from $\mathbf{J_i}$ is presented as the first 5 columns of (11) in [25].

A proper initial estimate must be used to start the iterations during solving (6) to guarantee fast convergence. Assuming the catheter motion is sufficiently slow and thus the magnet's position variation during the computational latency is small, a *warm start* strategy [30] is used in this work, where the optimal estimation of the current estimation is used as the initial condition of the next time step. Such an initialization strategy can facilitate the convergence of the L-M iteration and reduce the number of iterations required for convergence during real-time localization.

III. Calibration Algorithm

1) Ambient Field Removal

In our MSRC systems, the magnetic field from the source magnet at the sensor locations is below 8 Gauss, which is in the same order of magnitude as the earth's field. The ambient field signal must be removed from the sensor measurements to guarantee estimation accuracy. To achieve this, we first record the sensors' reading for earth's magnetic field without a magnet in the measurement range. This ambient field signal is then subtracted from the sensor readings in all sensor data to get the measurement of the field from the magnet. Note that the earth field measurement must be repeated if the system is being moved or rotated to maintain accurate magnetic localization.

2) Sensor Position and Magnetic Moment Calibration

In the magnetic localization approach shown in (6), the positions for all magnetic sensors $\mathbf{p_{si}}$ and the strength M of the PM to be localized are assumed to be known a priori. However, the actual sensor locations can deviate from their nominal locations due to inaccuracy in the mechanical design and assembly, and the discrepancy between the PM's strength and its nominal material properties. To address these issues, sensor data should be collected when the magnet is located at a series of known positions and orientations for calibration. One calibration approach introduced in [19] uses a sequential approach to estimate the magnet's dipole moment M and i-th

IEEE Robotics and Automation Letters (RA-L) paper, presented at ICRA 2024, Yokohama, Japan. Cite as RA-L paper.

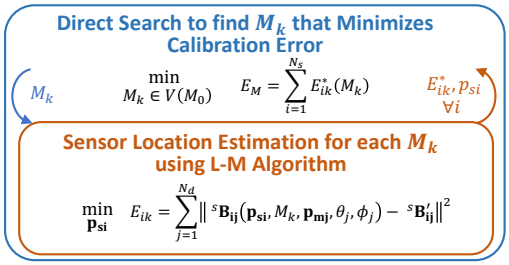

Fig. 4. The proposed new nested calibration method for magnetic dipole strength and sensor positions.

sensor location $\mathbf{p_{si}}$ as

$$\hat{M} = \arg\min_{M} \sum_{j=1}^{N_d} \sum_{i=1}^{N_s} \| M \ {}^s\bar{\mathbf{B}}_{\mathbf{ij}} - {}^{\mathbf{s}}\mathbf{B}'_{\mathbf{ij}} \|^2, \tag{8}$$

$$\hat{\mathbf{p_{si}}} = \arg\min_{\mathbf{p_{si}}} \sum_{j=1}^{N_d} \| {}^s\mathbf{B_{ij}}(\mathbf{p_{si}}, M, \mathbf{p_{mj}}, \theta_j, \phi_j) - {}^{\mathbf{s}}\mathbf{B}'_{\mathbf{ij}} \|^2, \tag{9}$$

where N_d is the number of all calibration data points, ${}^s\mathbf{B}'_{\mathbf{ij}}$ is the i-th sensor measurement for j-th calibration data, ($\mathbf{p_{mj}}$, θ_j, ϕ_j) are the position and orientation angles for the PM when taking the j-th data.

This problem solves for the optimal sensor locations that minimize the error between the estimated and true magnet locations. The nominal sensor locations are used to initiate the L-M iterations. Note that the optimal solution for dipole moment $\hat{M}$ obtained from (8) is used when solving for the sensor location estimation problem (9). This approach has demonstrated improvements in localization accuracy in [19]; however, due to the strong inter-dependency between the two optimization problems, a sequential calibration method in (8)-(9) can lead to sub-optimal calibration results. To remove the coupling between the two problems and achieve the optimal calibration results, ideally, the sensor location and magnetic dipole moment should be estimated simultaneously as formulated below

$$\min_{M, \mathbf{p_{si}}, \forall i} \quad E = \sum_{j=1}^{N_d} \sum_{i=1}^{N_s} \| M \ {}^s\bar{\mathbf{B}}_{\mathbf{ij}}(\mathbf{p_{si}}) - {}^{\mathbf{s}}\mathbf{B}'_{\mathbf{ij}} \|^2. \tag{10}$$

This optimization problem, however, is highly nonlinear and requires a large and highly-sparse Jacobian matrix with a dimension of $(N_s N_d) \times (3N_s + 1)$, which is computationally expensive and is impractical for sensor calibration.

Aiming to attain the overall optimal calibration results in sensor location and magnetic moment while maintaining computational simplicity, a new calibration approach is proposed in this paper as shown in Fig. 4. This proposed approach takes a nested framework to estimate the optimal magnetic dipole strength M and sensor locations $\mathbf{p_{si}}$. For each magnetic dipole moment value M_k in a feasible range $V(M_0)$ (around the vicinity of the nominal dipole strength M_0), the sensor location estimation problem (9) is solved for each M_k. The optimal magnetic dipole moment $\hat{M}$ can then be found through a direct search approach, which produces the minimum localization error over all sensors, and the optimal sensor positions $\hat{\mathbf{p_{si}}}$ can be found from the optimum in (9) with $\hat{M}$ being used. To speed up the computation, a coarse search can first be used to narrow the searching range, and a fine search can then be conducted to find the optimal M with sufficient accuracy. Compared with sequential estimation formulation in [19] and a simultaneous estimation formulation in (10), the proposed nested calibration approach (i) effectively addresses the coupling between two optimization problems, (ii) is computationally efficient, and (iii) can guarantee optimality [31]. The performance of the proposed new calibration approach is presented in Section VI.

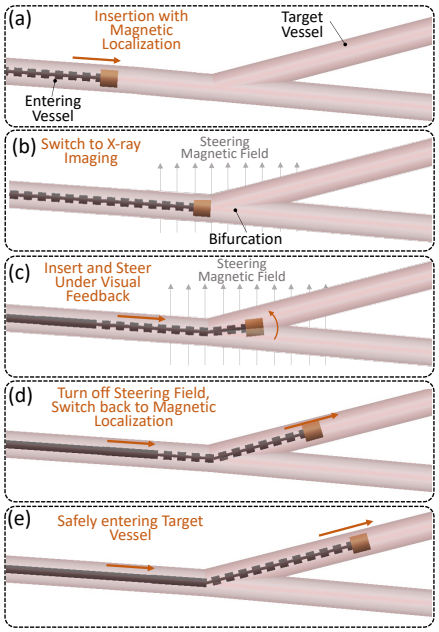

Fig. 5. Procedures of navigating a robotic catheter through a bifurcation in the vascular structure under a combination of magnetic steering, magnetic localization, and x-ray fluoroscopic imaging.

IV. Integrating Actuation and Localization

This section discusses the integration of the magnetic localization algorithm described in Section II and the magnetic steering for MSRC systems for PEI procedures. Due to the diameter constraint of catheters, the magnet at the catheter tip must have a diameter of 3 mm or smaller [21], and the magnetic sensors being used for the localization must be highly sensitive to capture the magnetic field from the catheter tip. However, such highly-sensitive magnetic sensors (e.g., magneto-resistive sensors for earth field measurement) typically have a relatively low measurement range. One example is the high-resolution magneto-resistive sensor QMC5883L, which has a high resolution of 5 mGauss but its measurement range is ± 8 Gauss. The magnetic actuation in MSRC systems typically exceeds 100 Gauss to steer the catheter tip, which will saturate the sensors and thus disable the magnetic localization. Hence, an integration method must be created to enable the smooth switching between magnetic steering (under x-ray fluoroscopic imaging guidance) and magnetic catheter tip tracking while minimizing x-ray radiation required to ensure safety during catheter navigation.

Figure 5 shows a schematic diagram for the proposed procedures for a robotic catheter to navigate through a bifurcation in the vascular structure under integrated magnetic steering and localization under the assistance of x-ray imaging only during steering. An x-ray image of the vascular structure is acquired before PEI therapy. During the PEI procedure, as the catheter is advanced into the straight segment of the vessel (Fig. 5a), magnetic localization is used to provide real-time feedback

IEEE Robotics and Automation Letters (RA-L) paper, presented at ICRA 2024, Yokohama, Japan. Cite as RA-L paper.

IEEE Robotics and Automation Letters (RA-L) paper, presented at ICRA 2024, Yokohama, Japan. Cite as RA-L paper.

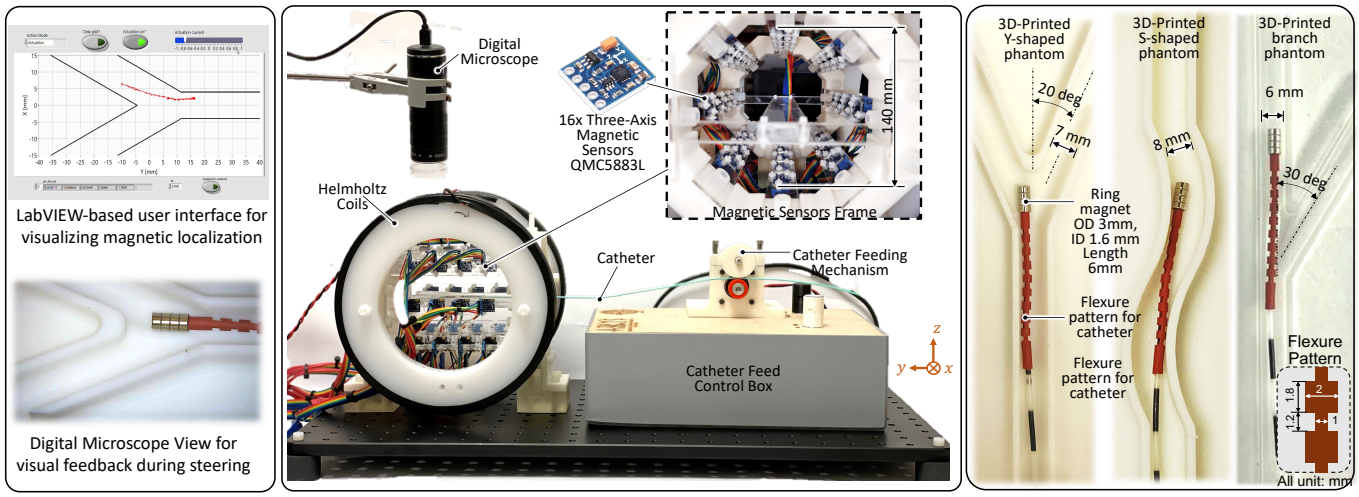

Fig. 6. Photograph of the magnetically steerable robotic catheter prototype system with magnetic localization for the catheter tip. Left: user interface for real-time visualization of magnetic localization result for catheter tip and digital microscope video for visual feedback during steering. Middle: hardware prototype comprising a catheter with a flexible distal segment and ring-shaped magnet adhered at its tip, Helmholtz coils for magnetic steering, a catheter feeding mechanism, a control box, a frame with 16 magneto-resistive sensors for catheter tip localization, a real-time controller for the system. Right: three 3D-printed phantoms for leg vasculature and catheter tip.

on the catheter tip location to the surgeon, and no steering field is needed. When the catheter tip comes to the proximity of the bifurcation, the localization method for the catheter switches to x-ray imaging, and a magnetic field is turned on to steer the robotic catheter towards the target branch (Fig. 5b-c). Once the catheter tip successfully select and is inserted in the proximal segment of the target branch, the steering field can then be turned off, and the localization of the catheter is switched back to magnetic localization, which guides further advancement of the robotic catheter towards the target lesion (Fig. 5d-e). A smooth transition between the magnetic steering (under x-ray imaging) and magnetic localization should be implemented to avoid sudden changes in the bending force for the catheter tip. Through this proposed procedure, fluoroscopic imaging in the navigation of an MSRC is significantly reduced to only bifurcation catheterization, which is highly effective in reducing the x-ray exposure to both the patient and surgeon during interventions.

V. Experimental Setup

Figure 6 shows an overview of the MSRC prototype system integrating magnetic steering and localization. The system comprises a catheter with a flexible distal end and magnetic tip, a steering actuator using Helmholtz coils, a catheter feeding mechanism, a magnetic sensor array for catheter tip localization, a digital microscope simulating the fluoroscopic imaging in PEI processes, and three different 3D-printed vasculature phantoms. The hardware design of the MSRC prototype (except for the magnetic localization system) is introduced in [21], which is briefly summarized below to make this paper self-contained. We then further discuss the design details for the magnetic localization system for the catheter tip.

The catheter being used in our prototype system consists of a commercially available catheter (G11430, Cook Medical, USA) and a flexible distal end made of a heat shrink tube (40142000, MILAPEAK) with 3.2 mm pre-shrinking outer diameter and 40 mm length. Flexure patterns are made on the catheter distal end to reduce its stiffness and thus increase steerability. The flexure pattern dimensions are shown in Fig. 6, and the modeling, design optimization, and fabrication procedures for the catheter distal end are presented in [32] and [21]. A stack of ring-shaped N52 NdFeB magnets with 3 mm outer diameter, 1.6 mm inner diameter, and a length of 6 mm is attached to the tip of the catheter to allow for magnetic steering and localization, as is shown in Fig. 6. The magnetic steering actuator being used is a pair of custom-fabricated Helmholtz coils aiming to create a uniform magnetic field for steering of the MSRC. The Helmholtz coils have a diameter of 220 mm and are configured with a distance of 110 mm. The coils are connected in series and are driven by full-bridge bi-directional switching-type power amplifiers (B07NP6XNPR, Cytron Technologies) with 20 A current capacity. The coils have 120 turns each under the maximum allowed current amplitude of 11 A (limited by the power supply being selected). The insertion of the catheter uses a feeding mechanism comprised of a friction drive driven by a stepper motor. The design details for the catheter feeding mechanism are discussed in [21].

In addition to the MSRC prototype system described above, a cylindrical array of magnetic sensors is arranged surrounding the catheter tip for localization, as is shown in Fig. 6. A high-resolution magneto-resistive sensor QMC5883L (5 mGauss resolution, measurement range ± 8 Gauss) is selected for the localization. In our prototype system, a total of 32 sensors are used for the cylindrical sensor array, and the y-directional distance between two sensors is 25 mm. The diameter of the cylindrical sensor array is 104 mm, aiming at the lower-limb treatment case. In this work, only 16 of the sensors (top, bottom, left, and right columns) are used for magnetic localization to allow for faster instrumentation and computation. Over-sampling is used for all sensor signals for noise reduction. The sensor signals are collected into a myRIO real-time controller (National Instruments) through I^2C interface via two 8-to-1 multiplexers. The latency for data collection is 5 ms. The real-

IEEE Robotics and Automation Letters (RA-L) paper, presented at ICRA 2024, Yokohama, Japan. Cite as RA-L paper.

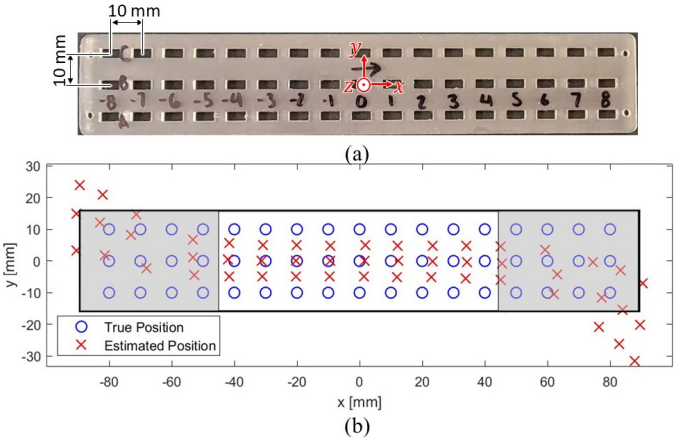

Fig. 7. Magnetic localization without sensor location calibration. (a) Photograph for the 3D-printed calibration plate I to place the magnet at varying defined locations. (b) Comparison between the true and estimated magnet locations using calibration plate I without sensor location calibration.

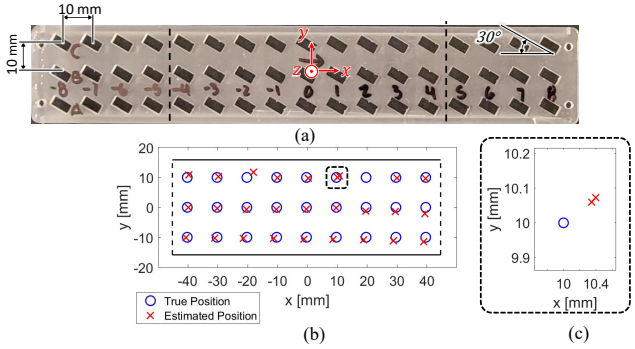

Fig. 8. Magnet location estimation data using an angled calibration plate after the sensor position and magnetic dipole strength calibrated using the proposed nested algorithm. Data in Fig. 7 are used for calibration. (a) Photograph of calibration plate. (b) Calibrated estimated magnet positions. (c) Zoom-in view for one out-lier data.

time magnetic localization and actuation algorithms discussed in Section II and IV are implemented in the myRIO real-time controller with a computation latency of approximately 400 ms, which is sufficiently fast for real-time feedback for the human operator.

VI. Results and Discussions

A. Magnetic Localization and Calibration Tests

To evaluate the localization performance and to calibrate the system, two different 3D-printed calibration grids are fabricated with a machining accuracy of 0.025 mm to place the PM being localized at different defined locations. We first collected the magnetic sensor readings with the magnet placed at all locations in the calibration plate (shown in Fig. 7a) and conducted magnetic localization using the measured data. Figure 7b shows the magnetic localization performance assuming the sensors are at their nominal locations. It can be observed that the magnet position estimation error is small when the magnet is within the center section of the plate, i.e., $x \in [-40\ \text{mm}, 40\ \text{mm}]$, and can reach 20 mm error when the magnet is at the edge of the calibration plate. This is because the magnet is out of the cylindrical sensor array when it is located at the front and back ends of the calibration plate, reducing the signal-to-noise ratio of sensor readings. To obtain high-quality signals and thus provide accurate localization performance, the sensor array must cover the magnet location.

Table I
AVERAGE LOCALIZATION ERROR WITH AND WITHOUT CALIBRATIONS.

Data Range	w/o calib.	w/ [19] calib.	w/ nested calib.
All (51 pts) xyz	10.16 mm	5.28 mm	4.53 mm
All (51 pts) $\theta\phi$	6.07°/12.48°	3.20°/8.52°	3.77°/8.62°
Center (27 pts) xyz	4.34 mm	1.74 mm	0.95 mm
Center (27 pts) $\theta\phi$	1.46°/3.84°	0.98°/3.08°	1.00°/1.75°

To improve the localization accuracy, the calibration for sensor location and magnetic dipole moment strength using the algorithm introduced in Fig. 4 was performed for our system. The data shown in Fig. 7 is used to perform the calibration. The computation time for the calibration problem solving is approximately 20 minutes on a regular desktop computer.

To validate the performance of the proposed sensor calibration procedure, a new calibration plate II (shown in Fig. 8a) was used. Localization was performed with the magnet placed at each location in the calibration plate II with and without the calibrations. Figure 8b shows the magnetic localization result after the calibrations, where there is an outlier in the boxed location shown in Fig. 8c. Table I summarizes the average translation and angular errors without calibration, using the method suggested in [19], and our proposed calibration method. It can be seen that the magnetic localization error in the center range (i.e., the region within the cylindrical sensor array, 27 points) is improved from 4.34 mm to 0.95 mm using the proposed method (i.e., a 45% improvement compared to the baseline approach). Moreover, Fig. 2 illustrates the magnetic localization performance comparison between this work and the prior studies, in which $V_m/|\mathrm{p_i}|$ is selected as the metric for the horizontal axis since the field from a magnetic dipole is proportional to this value. Thanks to the highly effective sensor calibration approach, our work demonstrates excellent overall performance in terms of accuracy and $V_m/|\mathrm{p_i}|$ compared to the previous literature.

B. MSRC Navigation Experiments

To demonstrate the effectiveness of the proposed integration of magnetic localization and magnetic steering in MSRC systems, experiments of navigating the catheter over three different 3D-printed phantoms of lower extremity vascular structure are conducted. The proposed switching procedure between magnetic location sensing and magnetic steering introduced in Section IV is used at bifurcation locations. During these case studies, a human operator can control the insertion and switch between magnetic steering and magnetic localization. Of note, in the envisioned procedure, the proposed magnetic localization was solely used to provide visual feedback to the user during the insertion procedure to minimize exposure to x-ray radiations, while the digital microscope video (simulating x-ray imaging) was used as the visual feedback during the magnetic steering step.

In this test, the catheter was first inserted into the top branch in the Y-shaped phantom with the operator under visual feedback using magnetic location sensing (Fig. 9a-d). Then, the catheter was retracted to the starting location (Fig. 9e) and switched to magnetic steering using the Helmholtz coils. In this step, the operator can control the steering field and catheter advancement under visual feedback from the digital microscope video (or under x-ray guidance) (Fig. 9f). After

IEEE Robotics and Automation Letters (RA-L) paper, presented at ICRA 2024, Yokohama, Japan. Cite as RA-L paper.

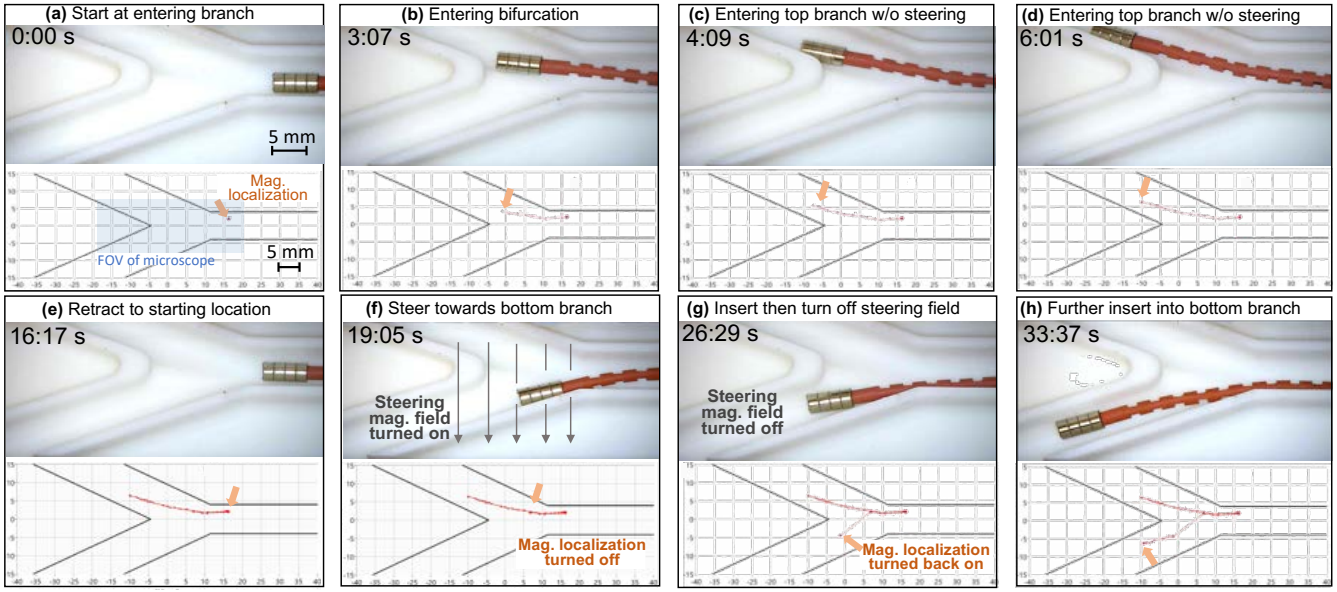

Fig. 9. Snapshots of digital microscope video for the prototype magnetically steerable robotic catheter navigating through the 3D-printed vascular phantom with 20 degree bifurcation and the screenshots of the user interface showing the catheter tip location estimation using magnetic localization.

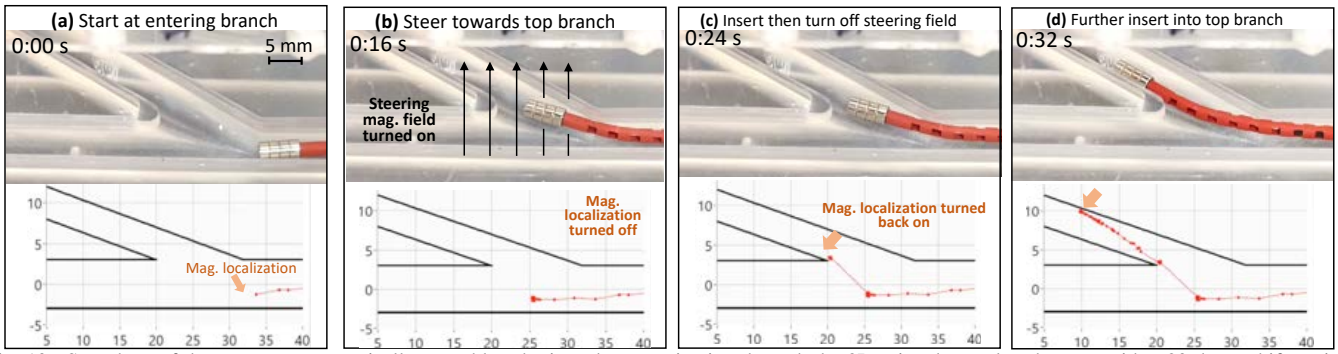

Fig. 10. Snapshots of the prototype magnetically steerable robotic catheter navigating through the 3D-printed vascular phantom with a 30 degree bifurcation.

the catheter enters the target branch, the operator can turn off the steering field and switch back to magnetic localization for catheter tip location sensing (Fig. 9g). Next, the operator can insert the catheter into the target branch under feedback using magnetic localization.

As shown in Fig. 10, an additional experiment of the catheter navigating through a 3D-printed phantom (with 6 mm diameter and 30 deg bifurcation) is used to mimic a realistic arterial. During these catheter navigation tests, the operator was able to successfully control the feed of the catheter while only looking at the user interface showing the magnetic localization result, and only needed to look at the digital microscope image during steering. These tests validate the effectiveness of the proposed method integrating magnetic steering and magnetic location sensing for MSRCs to minimize x-ray radiation for catheter navigation.

VII. Conclusions and Future Work

This letter introduces a new magnetic location sensing and actuation approach for magnetically steerable robotic catheters, aiming to reduce the x-ray exposure to the surgeon and the patient during intervention surgeries. The real-time magnetic location sensing uses the L-M algorithm to solve a least square estimation problem with 400 ms latency, which is sufficiently fast for visual feedback for the human operator during catheter insertion. This letter also introduces a new nested calibration framework for sensor locations and the dipole moment strength of the magnet, which addresses the coupling challenge in prior introduced sequential calibration approaches. To address the challenge that the actuation field can saturate location sensing sensors, we further proposed a novel integration approach for magnetic steering and magnetic location sensing, which reduce the need for x-ray usage to only at bifurcation locations. Experiments show that the magnetic location sensing error for a ring-shaped permanent magnet (3 mm OD, 1.6 mm ID, 6 mm length) over the sensing region is 1.27 mm, which well satisfies the required sensing accuracy. Catheter navigation tests verify the effectiveness of the proposed approach to integrating magnetic location sensing and magnetic steering for MSRCs.

Although satisfactory as a proof of concept, our proposed magnetic location sensing and steering methodology for robotic catheters require several improvements to unlock superior performance in practical vascular intervention applications: (i) Our proposed calibration algorithm (Fig. 4) only considers errors in sensor translational positions and magnet strength, and errors in sensor orientation are not considered. Future work should consider creating new calibration algorithms that address the coupled optimization for sensor loca-

IEEE Robotics and Automation Letters (RA-L) paper, presented at ICRA 2024, Yokohama, Japan. Cite as RA-L paper.

tion, orientation, and magnet properties, which is expected to enable further performance improvement in magnetic location sensing. (ii) The maximum deflection angle of the distal end of the current catheter is now limited to around 40 degrees. This can be further increased by developing a better flexure pattern or using a more flexible material for distal-end fabrication to reduce stiffness [32]. Besides, switching to a power supply with larger voltage and current capability can enlarge the maximum magnetic field and actuation torque generated from Helmholtz coils and thus improve the catheter's steerability. (iii) In the proposed integrated magnetic location sensing and steering method in MSRCs, x-ray imaging is still required for visual feedback during steering since the steering field saturates magnetic sensors for localization. To eliminate the need for fluoroscopic imaging during the catheter's navigation, our future work will consider developing model-based estimators of the catheter's location while magnetic localization is not available. We will also create a user interface that stitches the two location estimation seamlessly for feedback. (iv) Our current proof-of-concept prototype uses one pair of Helmholtz coils to steer the catheter in one lateral direction. A new catheter and magnetic actuation system including three pairs of Helmholtz coils should be designed in the future to enable the steering of the catheter in all directions (e.g., [33]). (v) Our current setup is built for testing lower-limb treatment cases. The performance of our sensing and actuation framework in a scaled-up system needs testing to adapt to more general cases. (vi) Experiments under fluid or blood conditions should also be tested in the future to simulate a more realistic situation. (vii) Aside from PAD treatment, there has been a rapid expansion of robotic interventions for cardiovascular and neurovascular procedures in recent years. Precise catheter localization systems aimed at these applications are suggested for future research and development efforts.

REFERENCES

[1] "Centers for disease control and prevision: Peripheral arterial disease (PAD)," https://www.cdc.gov/heartdisease/PAD.htm, accessed: February 19, 2023.

[2] U. Campia, M. Gerhard-Herman, G. Piazza, and S. Z. Goldhaber, "Peripheral artery disease: past, present, and future," *The American journal of medicine*, vol. 132, no. 10, pp. 1133–1141, 2019.

[3] M. H. Shishehbor and M. R. Jaff, "Percutaneous therapies for peripheral artery disease," *Circulation*, vol. 134, no. 24, pp. 2008–2027, 2016.

[4] "SwiftNINJA Steerable Microcatheter," https://www.merit.com/peripheral-intervention/delivery-systems/microcatheters/swiftninja-steerable-microcatheter, accessed: September 2021.

[5] M. Khoshnam and R. V. Patel, "Robotics-assisted control of steerable ablation catheters based on the analysis of tendon-sheath transmission mechanisms," *IEEE/ASME Transactions on Mechatronics*, vol. 22, no. 3, pp. 1473–1484, 2017.

[6] L. Wang, D. Zheng, P. Harker, A. B. Patel, C. F. Guo, and X. Zhao, "Evolutionary design of magnetic soft continuum robots," *Proc. Natl. Acad. Sci. U.S.A.*, vol. 118, no. 21, p. e2021922118, 2021.

[7] L. B. Kratchman, T. L. Bruns, J. J. Abbott, and R. J. Webster, "Guiding elastic rods with a robot-manipulated magnet for medical applications," *IEEE Transactions on Robotics*, vol. 33, no. 1, pp. 227–233, 2016.

[8] S. Zhang, M. Yin, Z. Lai, C. Huang, C. Wang, W. Shang, X. Wu, Y. Zhang, and T. Xu, "Design and characteristics of 3d magnetically steerable guidewire system for minimally invasive surgery," *IEEE Rob. and Auto. Letters*, vol. 7, no. 2, pp. 4040–4046, 2022.

[9] Z. Yang, L. Yang, M. Zhang, Q. Wang, S. C. H. Yu, and L. Zhang, "Magnetic control of a steerable guidewire under ultrasound guidance using mobile electromagnets," *IEEE Rob. and Auto. Letters*, vol. 6, no. 2, pp. 1280–1287, 2021.

[10] J. Edelmann, A. J. Petruska, and B. J. Nelson, "Magnetic control of continuum devices," *The International Journal of Robotics Research*, vol. 36, no. 1, pp. 68–85, 2017.

[11] F. Carpi and C. Pappone, "Stereotaxis niobe® magnetic navigation system for endocardial catheter ablation and gastrointestinal capsule endoscopy," *Exp. rev. of med. devices*, vol. 6, no. 5, pp. 487–498, 2009.

[12] B. L. Nguyen, J. L. Merino, and E. S. Gang, "Remote navigation for ablation procedures–a new step forward in the treatment of cardiac arrhythmias," *European Cardiology*, vol. 6, no. 3, pp. 50–56, 2010.

[13] J. Hwang, J.-y. Kim, and H. Choi, "A review of magnetic actuation systems and magnetically actuated guidewire-and catheter-based microrobots for vascular interventions," *Intelligent Service Robotics*, vol. 13, no. 1, pp. 1–14, 2020.

[14] T.-H. Chiang, Z.-H. Sun, H.-R. Shiu, K. C. Lin, and Y. Tseng, "Magnetic field-based localization in factories using neural network with robotic sampling," *IEEE Sensors J.*, vol. 20, no. 21, pp. 13 110–13 118, 2020.

[15] C. Hu, M. Q. Meng, and M. Mandal, "Efficient magnetic localization and orientation technique for capsule endoscopy," in *2005 IEEE/RSJ Int. Conf. on Intelligent Robots and Systems*. IEEE, 2005, pp. 628–633.

[16] S. Guitron, A. Guha, S. Li, and D. Rus, "Autonomous locomotion of a miniature, untethered origami robot using hall effect sensor-based magnetic localization," in *2017 IEEE International Conference on Robotics and Automation (ICRA)*. IEEE, 2017, pp. 4807–4813.

[17] D. Son, X. Dong, and M. Sitti, "A simultaneous calibration method for magnetic robot localization and actuation systems," *IEEE Transactions on Robotics*, vol. 35, no. 2, pp. 343–352, 2018.

[18] C. Watson and T. K. Morimoto, "Permanent magnet-based localization for growing robots in medical applications," *IEEE Robotics and Automation Letters*, vol. 5, no. 2, pp. 2666–2673, 2020.

[19] S. Su, W. Yang, H. Dai, X. Xia, M. Lin, B. Sun, and C. Hu, "Investigation of the relationship between tracking accuracy and tracking distance of a novel magnetic tracking system," *IEEE Sensors Journal*, vol. 17, no. 15, pp. 4928–4937, 2017.

[20] C. Heunis, J. Sikorski, and S. Misra, "Flexible instruments for endovascular interventions: Improved magnetic steering, actuation, and image-guided surgical instruments," *IEEE robotics & automation magazine*, vol. 25, no. 3, pp. 71–82, 2018.

[21] T. G. Mohanraj, J. Song, M. R. Rajebi, L. Zhou, and F. Alambeigi, "A kirigami-based magnetically steerable robotic catheter for treatment of peripheral artery disease," in *2022 9th IEEE RAS/EMBS Int. Conf. for Bio. Robotics and Biomechatronics (BioRob)*. IEEE, 2022, pp. 1–6.

[22] C. Fischer, T. Quirin, C. Chautems, Q. Boehler, J. Pascal, and B. J. Nelson, "Gradiometer-based magnetic localization for medical tools," *IEEE Trans. on Magnetics*, 2022.

[23] C. Fischer, Q. Boehler, and B. J. Nelson, "Using magnetic fields to navigate and simultaneously localize catheters in endoluminal environments," *IEEE Rob. & Auto. Letters*, vol. 7, no. 3, pp. 7217–7223, 2022.

[24] N. Sebkhi, N. Sahadat, S. Hersek, A. Bhavsar, S. Siahpoushan, M. Ghoovanloo, and O. T. Inan, "A deep neural network-based permanent magnet localization for tongue tracking," *IEEE Sensors Journal*, vol. 19, no. 20, pp. 9324–9331, 2019.

[25] C. R. Taylor, H. G. Abramson, and H. M. Herr, "Low-latency tracking of multiple permanent magnets," *IEEE Sensors Journal*, vol. 19, no. 23, pp. 11 458–11 468, 2019.

[26] S. Song, X. Qiu, J. Wang, and M. Q.-H. Meng, "Design and optimization strategy of sensor array layout for magnetic localization system," *IEEE Sensors Journal*, vol. 17, no. 6, pp. 1849–1857, 2017.

[27] M.-C. Kim, E.-S. Kim, J.-O. Park, E. Choi, and C.-S. Kim, "Robotic localization based on planar cable robot and hall sensor array applied to magnetic capsule endoscope," *Sensors*, vol. 20, no. 20, p. 5728, 2020.

[28] J. D. Jackson, "Classical electrodynamics," 1999.

[29] J. Shawash and D. R. Selviah, "Real-time nonlinear parameter estimation using the levenberg–marquardt algorithm on field programmable gate arrays," *IEEE Trans. on Ind. Elec.*, vol. 60, no. 1, pp. 170–176, 2012.

[30] J. Nocedal and S. J. Wright, *Numerical optimization*. Springer, 1999.

[31] J. Wu and L. Zhou, "Control co-design of actively controlled lightweight structures for high-acceleration precision motion systems," in *2022 American Control Conference (ACC)*. IEEE, 2022, pp. 5320–5327.

[32] Y. Liu, T. G. Mohanraj, M. R. Rajebi, L. Zhou, and F. Alambeigi, "Multiphysical analytical modeling and design of a magnetically steerable robotic catheter for treatment of peripheral artery disease," *IEEE/ASME Transactions on Mechatronics*, vol. 27, no. 4, pp. 1873–1881, 2022.

[33] D. S. Batista, F. Granziera, M. C. Tosin, and L. F. de Melo, "Three-axial helmholtz coil design and validation for aerospace applications," *IEEE Transactions on Aerospace and Electronic Systems*, vol. 54, no. 1, pp. 392–403, 2017.